Full length article

Surface-oxidized, freeze-cast cobalt foams: Microstructure, mechanical properties and electrochemical performance

Hyeji Park [a], Hoon-Hwe Cho [b], Kyungbae Kim [a], Kicheol Hong [a], Jae-Hun Kim [a], Heeman Choe [a], David C. Dunand [c, *]

[a] School of Materials Science & Engineering, Kookmin University, 77 Jeongneung-ro, Seongbuk-gu, Seoul, 136-702, Republic of Korea
[b] Department of Materials Science & Engineering, Hanbat National University, 125 Dongseodaero, Yuseong-gu, Daejeon, 305-719, Republic of Korea
[c] Department of Materials Science & Engineering, Northwestern University, 2220 Campus Drive, Evanston, IL, 60208, USA

A B S T R A C T

Cobalt with anisotropic open porosity is fabricated by directional solidification of aqueous slurries of nanometric Co_3O_4 powder where ice dendrites push powders into aligned interdendritic spaces, followed by ice sublimation, reduction of the oxide to metallic Co powders, and sintering of these Co powders into parallel lamellae. As the Co_3O_4 powder slurry fraction decreases (from 10 to 4 vol%), Co lamellae width in the final foam also decreases (from 93 to 8 μm) while foam porosity increases (from 66 to 85%). A drop in solidification temperature (from −10 to −50 °C) decreases porosity (from 77 to 63%) and lamellae width (from 11 to 5 μm) at a constant 8 vol% slurry fraction. Finally, with increasing sintering time (for −10 °C solidification temperature and 8% slurry fraction), Co foam porosity decreases (from 77 to 68%) and lamella width strongly increases (from 10 to 59 μm), consistent with sintering-induced coalescence of lamellae. The Co foams exhibit high strength but relatively low stiffness as compared to simple theoretical models, consistent with internal Co lamella buckling. A uniform Co oxide layer is grown by oxidation to create an active coating on the Co lamellae useful for lithium-ion storage. A coin-cell test carried out on the oxidized Co foam demonstrates a capacity (1283 mAhg^{-1}) almost twice that of a control oxidized Co foil anode, owing to its considerably larger surface area. Finite-element analysis is used to compute stresses and plastic strain evolutions during the lithiation process to understand the effect of oxide layer thickness and roughness, and micropores within the Co lamellae.

© 2017 Acta Materialia Inc. Published by Elsevier Ltd. All rights reserved.

1. Introduction

Because of its higher price as compared to iron- and nickel-based alloys, cobalt (Co) has found only niche structural applications [1,2] such as high-temperature superalloys [3], hard metal composites [4], and biocompatible alloy implants [2]. For non-structural applications, pure Co and Co-based alloys are widely used as catalysts (e.g., for electrochemical water oxidation) [3,4]. Co-based alloys are also considered potential alternatives to the scarce and expensive ruthenium- and iridium-based materials used in dye-sensitized solar cells (DSSCs) [5] and light-emitting electrochemical cells (LECs) [6] owing to their excellent physical, chemical, and mechanical properties. Co is also used, in its oxide forms, in functional applications in catalysts, magnetic storage

devices, supercapacitors, lithium-ion batteries (LIBs), and sensors [7,8]. For the above applications, cobalt (in pure, alloyed or oxidize form) with fine, interconnected porosity or channels can be used as an advanced functional "platform" material because of their high specific surface area, light weight, high toughness, high gas and liquid permeability, reduced thermal and electrical conductivity (compared to its bulk counterpart), and high stiffness- (and strength-) to-weight ratios [9—12].

The ice-templating method (also known as freeze-casting) can produce porous structures via simple, low-cost, scalable processing steps where powder slurry freezing followed by freeze drying is combined with powder sintering, as shown in Fig. 1a. When, as shown in Fig. 1b, the powder slurry is solidified directionally on the cold bottom surface of a mold, vertical colonies of parallel solid dendrites grow along the direction of the thermal gradient pushing the powder between the growing dendrites and creating powder-packed regions. When water is used as the carrier for the slurry,
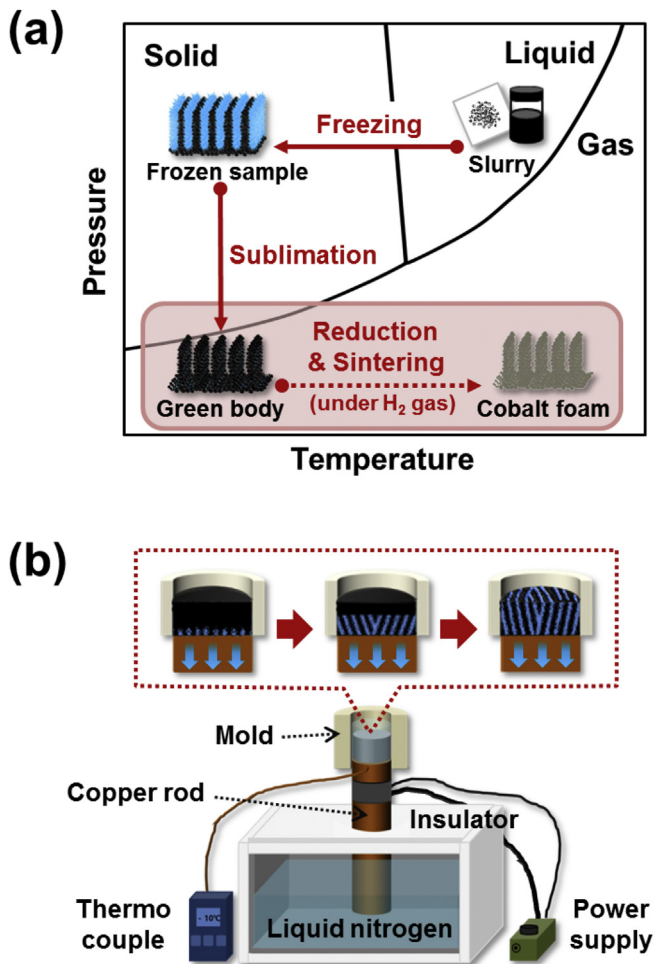
Fig. 1. (a) Schematic phase diagram of water illustrating phase changes in the liquid aqueous slurry during the ice-templating and sintering processes and (b) schematic illustration of ice-templating device and directional slurry freezing process.

highly anisotropic ice crystals (dendrites) grow along the thermal gradient. In a typical situation, the ice crystal growth occurs much faster along the "a" axis parallel to the thermal gradient than along the "c" axis perpendicular to the thermal gradient; however, the ice-crystal growth mechanism can be more complex in some situations. For example, the c-axis can also be parallel to the thermal gradient with the inclusion of an additive, which can affect the solidification parameters of the material system, such as the viscosity, surface tension, pH, freezing temperature, and interactions between the particles in suspension [13]. As the ice dendrites continuously grow along the temperature gradient, the solidification front velocity progressively decreases as it moves away from the mold bottom maintained at a constant temperature (as in a general set-up) and creates a microstructural gradient (e.g., with their thickness increasing to some extent), resulting in the formation of a structure composed of vertical lamellae of pure ice interspersed with regions rich in powders (Fig. S1) [14—16]. After full solidification, the ice dendrites are sublimated leaving directional pores, replicating the dendrites, surrounded by lamellae of packed powders. These are densified during a sintering step, thus forming a dense, three-dimensional porous material with elongated and aligned pores replicating the ice dendritic structure [14—26].

Ice templating has so far not only been applied to Co or its alloys, but a variety of porous ceramics and porous metals have been processed by the method [14—26], using for the latter metallic

powders (titanium) [18,23] or oxide powders that are chemically reduced to metal (copper [16], iron [26], nickel [24], and tungsten [27]) after the freeze-casting step. The ice-templating process can be used to tailor the size, porosity, orientation, and shape of pores with relative ease by controlling the particle characteristics, powder content in the slurry, slurry solidification direction and velocity, and sintering time and temperature [14,19,21,25]. Due to their affordability and ease of fabrication, ice-templated porous metals, with their unique open directional structures with large surface areas, dense lamellae, and good mechanical properties, show promising potential for use as structural materials, as well as functional materials such as biomaterials, catalysts, sensors, and electrodes [14].

Although several forms of Co have been manufactured and reported for use in functional applications in the form of foil, nanopowder, nanowire, 3D-printed porous architecture [28], and sintered powder [29], we describe here for the first time the fabrication and structure of porous Co with a well-defined lamellar structure obtained by optimizing the primary processing parameters for the ice-templating process. We synthesize a porous green body using Co oxide (Co_3O_4) powders, and then reduce and sinter it to produce porous metallic Co. This study discusses the effects of powder slurry fraction, slurry solidification temperature and sintering time on the morphology of the synthesized Co foams. The compressive mechanical properties of selected Co foam samples are measured and compared with theoretical models.

Additionally, a representative Co foam, after thermal oxidation to form a Co oxide layer on its surfaces, is demonstrated as an anode of LIBs. This is because Co oxides, such as Co_3O_4 and CoO, are well known as high-capacity anode electrode materials for LIBs [30—34]. Finite element analysis (FEA) is then applied to examine the stress state developed in the Co/Co oxide foam during (de)lithiation associated with (dis)charging.

2. Experimental procedures

2.1. Sample preparation

A powder slurry was created by suspending 4 to 12.5 vol% Co oxide (Co_3O_4) nanoparticles (size ~30 nm, 99.9% purity, Inframat Advanced Materials, USA) in 5 ml deionized water, and 6.5 wt% polyvinyl alcohol (PVA, Sigma-Aldrich Co., USA, fraction calculated with respect to the Co_3O_4 powder) was added as a binder. The slurry was homogenized by a combination of stirring and sonication lasting ~150 min at ambient temperature, and then poured into a Teflon mold (20 mm inner diameter, 21 mm outer diameter, 25 mm height) whose bottom surface was a copper rod cooled at its lower end with liquid nitrogen. Using a resistive heater along the length of the rod, the temperature of its upper surface (forming the bottom of the mold) was maintained at −10, −30, or −50 °C. The strong thermal gradient within the slurry after pouring led to the vertical growth of ice crystals and rejection of suspended oxide particles to interdendritic space. The fully solidified slurry with a height of 14 mm was then sublimated, in a vacuum, at −88 °C for 24 h in a freeze dryer (Operon, FDU—7003, Republic of Korea), resulting in an oxide green body with directional pores replicating the sublimated dendrites. This green body was heated in a tube furnace, under a flowing Ar-5% H_2 gas mixture, to two consecutive temperatures: (a) 550 °C for 4 h to remove the binder and chemically reduce Co_3O_4 to Co and (b) 900 °C for 1.5, 2.5, or 4 h to sinter the metallic Co. Heating and cooling rates were 5 and 3 °C min^{-1}, respectively.

In a first series of experiments (sintering time control), slurries with 8 vol% Co_3O_4 powder were directionally solidified at a fixed copper rod temperature of −10 °C. After freeze drying and pre-

sintering at 550 °C for 4 h (for debinding and reduction), sintering at 900 °C was carried out for 1.5 h (sample labeled S1.5), 2.5 h (S2.5), and 4 h (S4).

In a second series of experiments (oxide powder volume control), the volume fraction of oxide powder in the slurry was varied from 4 to 12.5 vol% (i.e., 4, 6, 8, 10, 11, and 12.5 vol%). All slurries were frozen at a fixed copper rod temperature of −10 °C. After freeze drying, the green bodies (labeled respectively V4, V6, V8, V10, V11, and V12.5) were pre-sintered at 550 °C for 4 h (for binder removal and powder reduction) and sintered at 900 °C for 1.5 h.

For a third series of experiments (solidification temperature gradient control), the temperature of the copper rod was changed from −10 °C (T10) to −30 °C (T30) and −50 °C (T50), thus increasing the solidification temperature gradient. The slurries consisted of 8 vol% Co_3O_4 powder. After the same freeze-drying and pre-sintering steps used in the previous experiments, the slurries were sintered at 900 °C for 1.5 h.

2.2. Material characterization

The microstructure and composition of all samples synthesized by controlling the three main processing parameters were characterized by optical microscopy (PME 3, Olympus, Japan), X-ray diffraction (XRD, Rigaku, DMAX2500, Japan), and field-emission scanning electron microscopy (FE-SEM, SU8030, Hitachi, Japan). Overall porosity was calculated by considering the theoretical density of bulk Co (8.90 g/cm³) and by measuring its mass and calculating its volume from height and diameter measurements. In the second method, the bulk porosity was also determined using the Archimedes method with water as the immersion fluid to estimate the closed porosity present in the strut walls of the Co foams. Co foam lamella thickness was measured by a line intercept method on cross-sections cut parallel to the direction of the temperature gradient. Parallelepiped compression specimens were machined with 3 mm sides and 6 mm heights oriented parallel to the freezing direction in an attempt to avoid the initial transition zone at the bottom of the sample (Fig. S2). Compressive tests were carried out using an extensometer at a nominal strain rate of 0.001 s⁻¹ on three series of samples with varying porosity (V4, V8, V10, and V12.5) and different morphologies (S4, T30, and T50) using a calibrated universal testing machine.

2.3. Application and electrochemical characterization of Co foam as an anode in LIB

The synthesized Co foam (V8: 8 vol% Co_3O_4, −10 °C) was cut into coin samples 300 μm thick to be used as an anode current collector. To grow a Co oxide layer on the surface of the Co foam coin sample, the Co foam sample was heat treated at 600 °C for 10 min in an electric furnace in air. In order to examine the effect of porous architecture on the electrochemical performance of the Co foam, Co foil (99.9% purity, Alfa Aesar) was also prepared for comparison using the same conditions. The microstructure and composition of the integrated Co_3O_4/CoO/Co anode were characterized using XRD (Rigaku, DMAX2500, Japan), FE-SEM (JSM7610F, JEOL, Japan), and electron dispersive X-ray spectroscopy (EDX).

The electrochemical performance of the prepared Co foam coin sample, without the use of a binder and conductive materials, was evaluated by a standard coin-cell test assembled in an Ar-filled glove box. The working electrodes were cut into disc coupons approximately 11 mm in diameter and 300 μm in width. Li foil was used as both the counter and reference electrodes. The tests were carried out with CR2032 coin-type half cells using 1.0 M LiPF6 in a solution of ethylene carbonate (EC)/diethyl carbonate (DEC) (3:7 vol ratio, PANAX Etec), which was used as the electrolyte with a porous polypropylene separator (Asahi Kasei Chemicals). The cells were tested galvanostatically at a constant current of 100 mA/g in the voltage window between 3.0 V and 0.01 V vs. Li+/Li at 25 °C on a battery test system (CTS-Lab, BaSyTec, Germany).

2.4. Finite element modeling

The governing equations of deformation and diffusion in the electrode, which are implemented in the ABAQUS/Standard software incorporating a user-defined subroutine, have already been discussed elsewhere [35,36]. In this finite element (FE) model, the equations can be solved sequentially for diffusion and mechanical deformation. In other words, Li concentrations extracted from the diffusion computation are subsequently passed to the mechanical deformation computation.

A representative volume element (RVE) of the Co foam with Co oxide was created, as illustrated in Fig. 2. The RVE consisted of the Co_3O_4 active layer (0.5 μm thickness) and the Co scaffold with a bridge where the Co lamellae and the bridge are connected (Fig. 2a). It was assumed that no CoO is present. The RVE had 12,413 tetrahedral elements consisting of Co_3O_4 (6312 elements) and Co (6101 elements), as shown in Fig. 2a. To examine the effect of geometrical modification of the Co lamella thickness on the mechanical behavior, an RVE with a 0.25-μm thin active layer (i.e., half the 0.5-μm thickness in Fig. 2a) was also created along with roughness and pores, as seen in Fig. 2b−d, where the RVE had 11,441 (Co_3O_4 and Co: 5340 and 6101 elements), 13,216 (Co_3O_4 and Co: 6782 and 6434 elements), and 12,234 elements (Co_3O_4 and Co: 6312 and 5922 elements), respectively. The boundary conditions resulting from the electrochemical reactions were enforced in the RVE. The initial condition was $c = 0$ at $t = 0$ at all locations. During operation, a Li-ion concentration, c_s, on the electrode surface could be determined from the electrode voltage so that the concentration of Li-ion on the surface during lithiation was set as $c = c_s$ on the surface of the electrode for lithiation. For delithiation, the simulation started with the fully lithiated state. Since the discharging rate is the same as the charging rate, the flux boundary condition was adjusted from in-flux to out-flux at the same magnitude. The RVE was considered to have mirror boundary conditions along x, y and z directions to enforce periodic boundary conditions and create a lamellar structure with perpendicular bridges. The material properties of Ni_3Sn_2 and Ni taken from Ref. [35] were employed for the parameter values in this study, because there have been very few measured data available for the lithiation process. The replacement of the materials properties of CoO/Co_3O_4 and Co with those of Ni_3Sn_2 and Ni is considered reasonable for a semi-quantitative analysis. More details of this modeling procedure can be found in Ref. [35]. Here, we used the stress-strain curves of Ni_3Sn_2 and Ni in the FE modeling, using yield points of 633 and 600 MPa, respectively [35].

3. Results and discussion

3.1. Microstructure

Table 1 summarizes the ten specimens studied, which are arranged by experimental series based on the three experimental variables (sintering time, powder fraction in slurry, and solidification temperature). Specimens S1.5, V8, and T10 are the same but labeled differently according to their own series. Table 1 also lists the two main measured microstructure parameters: foam porosity and Co lamella thickness. In particular, closed porosity is also estimated by measuring the "apparent density", as measured using the Archimedes method, which is the density of Co walls containing small, closed pores. The apparent density is divided by the
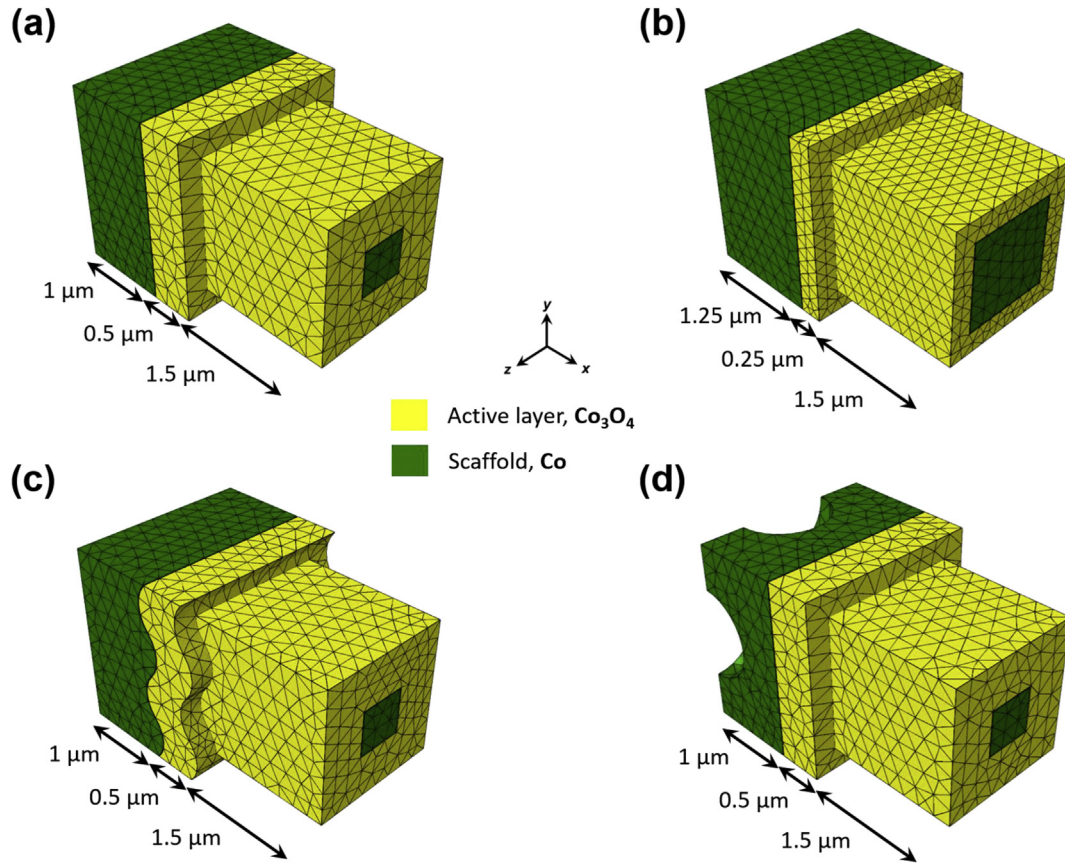
Fig. 2. 3D mesh structures of the representative volume element (RVE) for Co foam with Co oxide layer grown (mirror boundary conditions in all directions): (a) thick oxide layer, (b) thin oxide layer, (c) thick oxide layer with roughness, and (d) thick oxide layer with pores.

Table 1
List of foam specimens showing the three main processing parameters (fraction of Co_3O_4 powder in slurry (vol%), slurry solidification temperature (°C), and foam sintering time (h)) and the two main microstructural parameters (Co lamella thickness and foam porosity). Specimens S1.5, V8 and T10 are the same.

Processing parameter	Experimental Condition						
	Sample	Fraction of Co_3O_4 Powder (vol%)	Solidification temperature (°C)	Sintering time (h)	Lamella thickness (μm)	Porosity (%)	
						Open	Closed
Sintering time	S1.5	8	−10	1.5	11 ± 1	77.4 (70.5/6.9)	
	S2.5	"	"	2.5	15 ± 2	76.4 (72.5/3.9)	
	S4	"	"	4	59 ± 2	67.8 (62.3/5.5)	
Powder fraction in slurry	V4	4	−10	1.5	8 ± 2	85.1 (83.1/2.0)	
	V6	6	"	"	12 ± 3	77.9 (71.9/6.0)	
	V8	8	"	"	11 ± 4	77.4 (70.5/6.9)	
	V10	10	"	"	93 ± 8	66.0 (56.8/9.2)	
	V11	11	"	"	134 ± 4	57.4 (52.6/4.8)	
	V12.5	12.5	"	"	732 ± 8	56.3 (45.7/10.6)	
Solidification temperature	T10	8	−10	1.5	11 ± 1	77.4 (73.4/4.0)	
	T30	"	−30	"	7 ± 2	68.0 (66.0/2.0)	
	T50	"	−50	"	5 ± 4	63.4 (56.1/7.3)	

theoretical Co density to determine the closed porosity, which varies from 2.0% to 10.6% (Table 1). The amount of closed porosity appears to decrease with increasing sintering time and increase with increasing powder fraction, (Table 1), although occasional defects and irregularities in the Co samples makes these conclusions somewhat speculative.

The chemical reduction and sintering steps at high temperature caused a significant reduction of the dimensions of the Co oxide green-body samples because of the removal of oxygen during reduction and the densification of the metallic powders during sintering. For sample S1.5, the overall volumetric shrinkage was measured as $\Delta V/V \sim 82\%$, with radial and height shrinkages being $\Delta r/r \sim 36\%$ and $\Delta h/h \sim 43\%$, respectively, resulting in near-isotropic shrinkage, despite some visible cracks observed parallel to the temperature gradient in a few samples (see Fig. S3 for a representative sample with a few visible cracks along the temperature gradient presumably developed during reduction and sintering). Both the magnitude and isotropy of shrinkage were in agreement with previous studies where directionally freeze-cast CuO [16], NiO [24], and WO_3 [27] specimens were reduced and sintered.

Fig. 3 shows SEM micrographs of a representative Co foam (V8: 8 vol% Co_3O_4, $-10\ ^\circ C$ freezing temperature). The elongated aligned lamellae, $13 \pm 2\ \mu m$ in thickness, and the directional lamellar pores, $20 \pm 4\ \mu m$ in width, can clearly be seen in the corresponding SEM images (Fig. 3a–e). Noteworthy is the presence of much smaller secondary surface pores, creating corrugated surfaces on only one side of the Co lamellae, with the other side being relatively flat (Fig. 3b, d, e). This is because ice dendrite growth is generally tilted

a few degrees with respect to the direction of the temperature gradient upon freezing. As a result, small secondary dendrite arms, a few micrometers in length, form on one side of the ice crystals toward the direction of the temperature gradient but not on the other side, creating the surface porosity or corrugation, as reported also in other prior publications [37,38].

3.2. Effect of sintering time on microstructure

Fig. 4a–f shows optical micrographs of the radial and longitudinal sections of the ice-templated Co foams for different sintering times: (a, d) 1.5 h for S1.5, (b, e) 2.5 h for S2.5, and (c, f) 4 h for S4. All micrographs, which are representative of the entire samples, show the expected morphology of colonies of aligned, lamellar macropores replicating ice dendrites surrounded by Co lamellae. As expected for a porous metal undergoing sintering, the overall porosity of the samples decreased from 77.4 to 76.4 to 67.8% with increasing sintering time from 1.5 to 2.5–4 h, respectively, as shown in Fig. 7a. The mean Co lamella thickness increased from 10.3 ± 0.9 to 15.3 ± 1.5 to $59.1 \pm 2\ \mu m$ for sintering times increasing from 1.5 to 2.5–4 h, respectively, as shown in Fig. 7a. Considering an individual porous lamella, increased sintering time is expected to reduce its thickness, as internal pores are eliminated. On the other hand, the observed trend implies that neighboring lamellae coalesced, resulting in a near quadrupling of lamella thickness (from 15.3 ± 1.5 to $59.1 \pm 2\ \mu m$) as sintering time was increased from 2.5 to 4 h (Fig. S4); this is quite a drastic increase, especially since the initial increase in lamella thickness was modest (10.3 ± 0.9 to
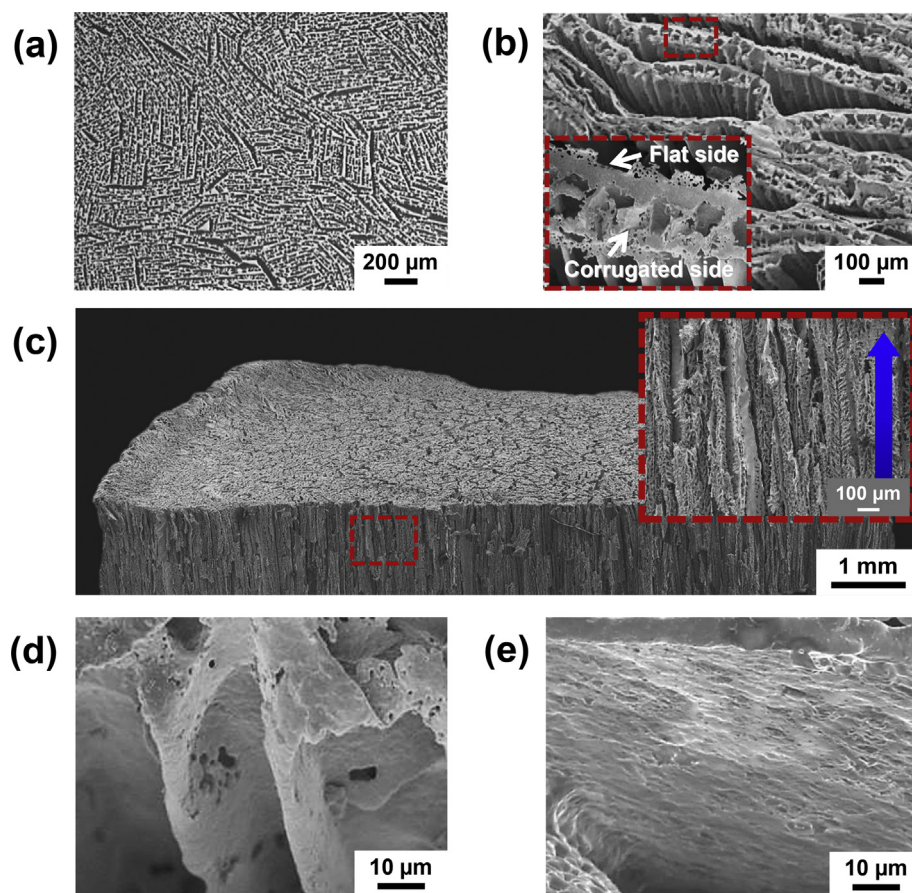
Fig. 3. SEM micrographs of (a, b) radial section and (c–e) longitudinal section of the ice-templated Co foam S1.5 (also labeled V8, T10) with 8 vol% Co_3O_4, solidification temperature $-10\ ^\circ C$, sintering time 1.5 h. Only one side of the lamellae exhibits corrugations created by secondary ice dendrites, possibly as a result of competition between the temperature gradient and the preferred ice growth direction as indicated by arrows in (b): (d) corrugated side and (e) flat side.
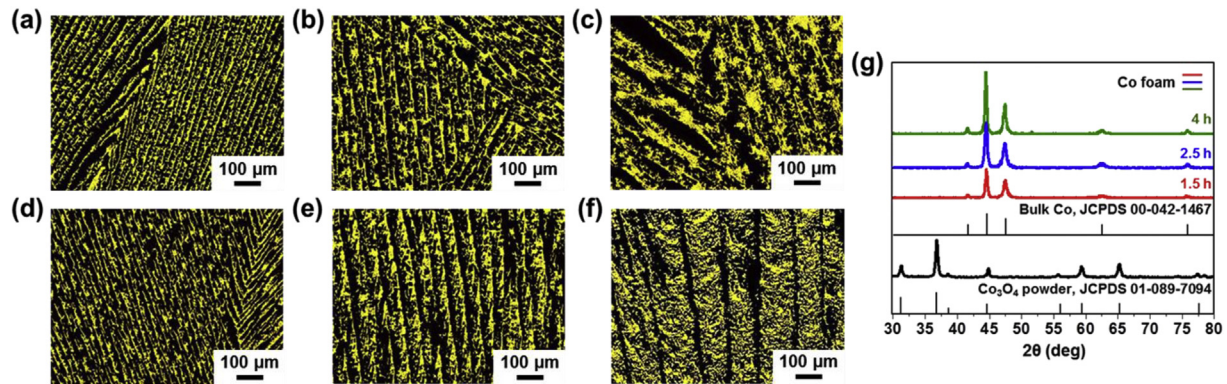
Fig. 4. Optical micrographs of (a–c) radial and (d–f) longitudinal sections of Co foams (Co$_3$O$_4$ powder fraction ~8 vol%; solidification temperature −10 °C with the vertical solidification direction) sintered for various times: (a, d) 1.5 h (S1.5), (b, e) 2.5 h (S2.5), and (c, f) 4 h (S4). (g) XRD patterns of Co oxide powder and ice-templated Co foams for three sintering times (S1.5, S2.5, and S4).

15.3 ± 1.5 μm) when sintering time increased from 1.5 to 2.5 h. The unusually large increase in the lamella thickness is in good agreement with the considerable sample shrinkage observed between the sintering times of 2.5–4 h (Fig. S4); however, a typical sintering mechanism may not well explain the drastic quadruple increase in the lamella thickness, because Co lamella walls are somewhat less well defined in this study than the lamella walls observed in other ice-templated metal foam systems such as Cu [16] and Ni [24]. The dramatic increase in lamella thickness is indeed considered as the increase in an "effective" lamella thickness. In other words, the initial elimination of internal and surface lamella pores appears to be associated with insignificant lamella thickness change, whereas the coalescence of neighboring lamellae in the later sintering stage is likely to be associated with the increase in an "effective" lamellar thickness with increasing sintering time. The mass of the reduced and sintered samples decreased by $\Delta m/m = 32 \pm 0.4\%$ (averaged over all samples), calculated to be from oxide reduction (26% decrease) and burn-off of the PVA binder (6% decrease). XRD pattern analysis also confirmed that the three samples T1.5, T2.5, and T4 were completely reduced from Co$_3$O$_4$ to Co, as shown in Fig. 4g.

3.3. Effect of slurry powder concentration on foam microstructure

The effect on the foam microstructure of increasing the powder fraction in the slurry from 4 to 12.5 vol% is illustrated in Fig. 5a–l. The porosity of the Co foams decreased from 85.1 to 56.3% for powder slurry concentrations increasing from 4 to 12.5 vol%, as reported for each sample in Table 1 and as shown in Fig. 7b. This trend is expected, as the porosity of the oxide green body, and thus of the sintered Co foam, is directly related to the volume fraction of dendritic ice in the frozen composites, and thus water in the original slurries [38].

The foams created from the three lowest oxide concentrations in the slurries (4, 6, and 8 vol%) exhibited the typical lamellar structure of freeze-cast materials with parallel, elongated pores replicating ice dendrites aligned along the solidification temperature gradients. The sintered metallic lamellae had the same morphology as those shown in Fig. 3b, flat on one side and corrugated on the other, as reported in Ref. [38]. By contrast, the three foams solidified from slurries with higher volume fractions of Co$_3$O$_4$ nanoparticles (10, 11, and 12.5 vol%) showed much thicker Co lamellae with smaller, irregularly distributed pores in thick struts. The longitudinal and radial sections were similar to those exhibited by the sample S4 (Fig. 4c and f) with thick lamellae of partially sintered powders, showing no flat/corrugated asymmetry. It is thus possible

that the same phenomenon, lamella coalescence, is responsible for the drastic increase in lamella thickness (from 11 to 93 μm) as the slurry Co$_3$O$_4$ fraction increased modestly (from 8 to 10 vol%), as shown in Fig. 7b. The onset of lamella coalescence is indeed expected to occur sharply, as either sintering time (Fig. 7a) or slurry particle fraction increases (Fig. 7b) beyond a threshold value.

Another explanation for the drastic change in lamella thickness and morphology may be a "breakthrough" as the solid/liquid interface breaks into the slurry at the critical concentration, as previously described by Shanti et al. [22]. In other words, the breakthrough is driven by the competition between the capillary force pushing the particles and the osmotic pressure allowing water to permeate the collected particles. Furthermore, it is possible that the dendrites engulfed rather than pushed the particles, a phenomenon that is mostly affected by solidification velocity. While the thermal conductivity of the slurry (and thus freezing velocity) is affected by the particle fraction, it is unlikely that early engulfment explains the very thick lamellae seen in Fig. 5, as the oxide particles were nanometric and could thus be easily pushed by growing ice dendrites. However, particle clumping could have also taken place, especially due to magnetic interaction of the Co oxide particles, increasing the effective particle size to the point that early engulfment may have occurred in samples V10–V12.5. The effective particle size is closely associated with the critical ice front velocity, above which particle engulfment tends to take place [18]. Despite the relatively slow ice front velocity, estimated to be ~10 μm/s in our case, the heavily agglomerated Co oxide particles could increase in size up to several tens of micrometers to trigger the particle engulfment phenomenon (Fig. S1). In particular, the sample V12.5 with the highest amount of powder loading (Fig. SI) appears to exhibit "ice banding (ice lenses)", a pattern of alternating macroscopic layers of ice (pores) and particles perpendicular to the temperature gradient. These features of ice lenses were previously observed in frozen colloidal dispersions [39] and ice-templated ceramics [38,40].

3.4. Effect of slurry solidification temperature on microstructure

Fig. 6 shows optical micrographs of ice-templated Co foams with different solidification temperatures: (a–c) −10 °C (T10), (d–f) −30 °C (T30), and (g–i) −50 °C (T50), all taken at the same height within the samples (at the two-third position of the sample height from its bottom as shown in Fig. S5). It is apparent from these micrographs that a finer microstructure (smaller pores and thinner lamella struts) was achieved with a lower solidification temperature and faster freezing rate, in good agreement with
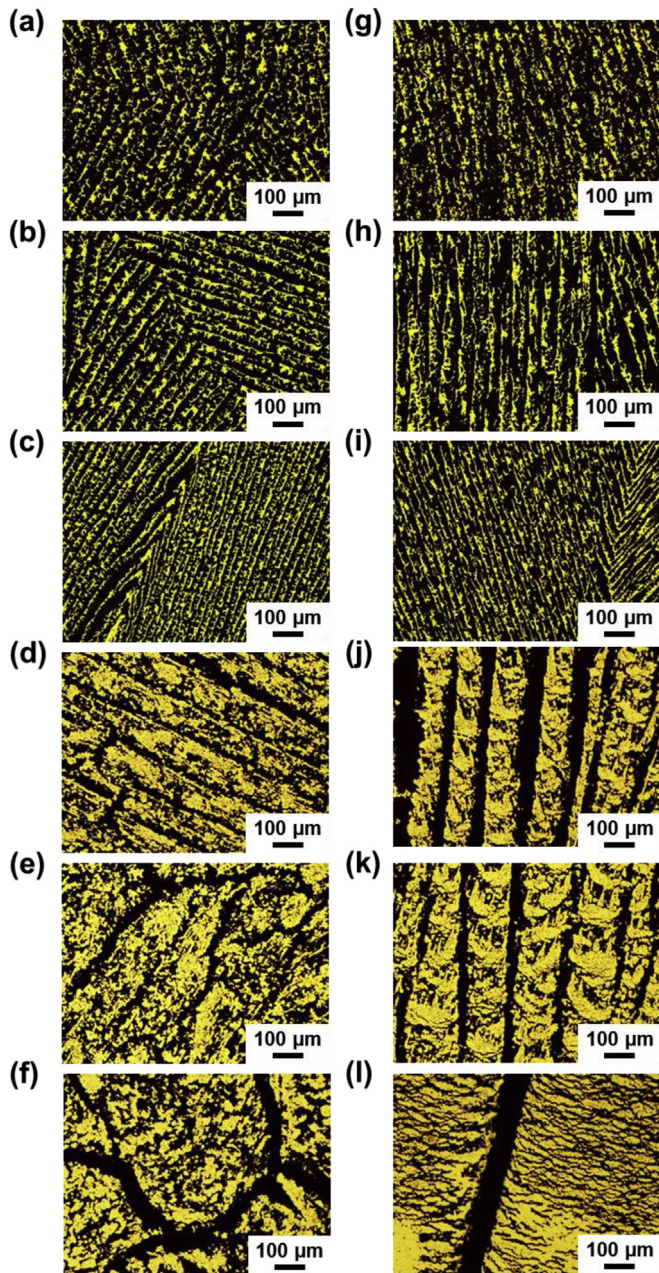
Fig. 5. Optical micrographs of (a–f) radial and (g–l) longitudinal sections of Co foam (solidification temperature −10 °C; sintering time 1.5 h) with varying oxide slurry fraction: (a, g) 4 vol% (V4), (b, h) 6 vol% (V6), (c, i) 8 vol% (V8), (d, j) 10 vol% (V10), (e, k) 11 vol% (V11), and (f, l) 12.5 vol% (V12.5).

previous reports [14,16]. Because ice nucleation is enhanced as the supercooling increases, an inverse relationship between the lamella width and the velocity of the ice front was previously observed on freeze-cast Cu foam [16] and some other systems [38,41,42]; in other words, with lower casting temperature, more numerous and thinner dendrites are created, leading to thinner lamellar macropores and lamellae.

As reported in previous studies [14,17] in which the ice front morphology changed from a planar to a columnar and finally to a lamellar shape during the freeze casting of porous alumina with decreasing solidification velocity (i.e., with increasing distance from the cold bottom surface or decreasing slurry solidification temperature), our Co foams also seemed to show a similar

morphological evolution. At −30 °C, the most representative morphology appeared similar to a columnar structure due to the faster ice growth velocity (see Fig. 6d–f). At −50 °C, a much finer, random porous structure was obtained in both the radial and longitudinal directions without any apparent directionality (see Fig. 6g–i). Suspension supercooling has a significant influence on both the ice nucleation and crystal growth rates, and there is a competition between the ice nucleation and growth depending on the degree of supercooling. In other words, for a higher supercooling at a lower solidification temperature, the ice nucleation rate dominates, resulting in the formation of a larger number of small ice crystals, leading to small uniform pores in the sintered foam. By contrast, if the degree of supercooling is lower at a higher solidification temperature, ice growth dominates, resulting in a smaller number of larger ice dendrites, forming large directional pores in the sintered foam [41]. Indeed, both the porosity and lamella width were observed to decrease with decreasing solidification temperature (i.e., increasing degree of supercooling effect), as illustrated in Fig. 7c.

3.5. Effect of microstructure on compressive behavior

Co foams with different porosities (V4, V8, V10, and V12.5) or pore morphologies (lamellar for S4, columnar for T30, and near-equiaxed for T50) were deformed in compression, with the loading axis parallel to the longitudinal pore direction as schematically shown in Fig. 8a. All specimens exhibited the three regimes of compressive deformation typical of ductile porous metals (i.e., an initial linear elastic region, a plastic plateau where stress values fluctuate, and finally a densification regime with steeply rising stress values) [18,23,43]. It is apparent that porosity has a great influence on the compressive strength of the Co foams. Indeed, the compressive strength of Co foams increased by over an order of magnitude, from 4 to 64 MPa, when the porosity decreased from 85.0 to 56.3% (Fig. 8a).

Remarkably, the shape and directionality of the pores also has a considerable effect on the compressive strength, as shown in Fig. 8b. Given the same volume fraction of Co_3O_4 powder in the slurry (8 vol%) and a similar Co foam porosity (68%), specimen T30 with columnar/prismatic Co scaffold shows a compressive strength threefold higher than specimen S4 with lamellar Co scaffold/pore architecture (65 vs. 23 MPa). Additionally, the compressive strength of specimen T30 (65 MPa) was even higher than that of specimen T50 (48 MPa) with nearly random pore structure despite its lower porosity (63.4%). Similar stress-strain curves have been published for copper foams directionally freeze-cast from its oxide powder, confirming the importance of pore directionality and morphology [16]. Compressive tests on the specimens of a directional Cu foam (p = 63%) with the uniaxial loading direction parallel and perpendicular to the Cu lamella orientation revealed that the yield strength is also threefold higher (43 vs. 14 MPa) when lamellae are oriented parallel to the loading axis [16].

Fig. 9a and b shows, in double logarithmic plots, the effect of foam relative density on the foam yield strength (9a) and Young's modulus (9b), along with Gibson−Ashby (G−A) and cellular−lattice−structure−in−square−orientation (C−L) predictions. First, the yield strength and the Young's modulus of the G−A model are presented as described by Eqs. (1) and (2) [44].

$$\sigma^* \approx \sigma_{Co} C_1 \rho^{*3/2} \tag{1}$$

$$E^* \approx E_{Co} C_2 \rho^{*2} \tag{2}$$

where σ_{Co} is the yield strength of annealed Co (taken as either
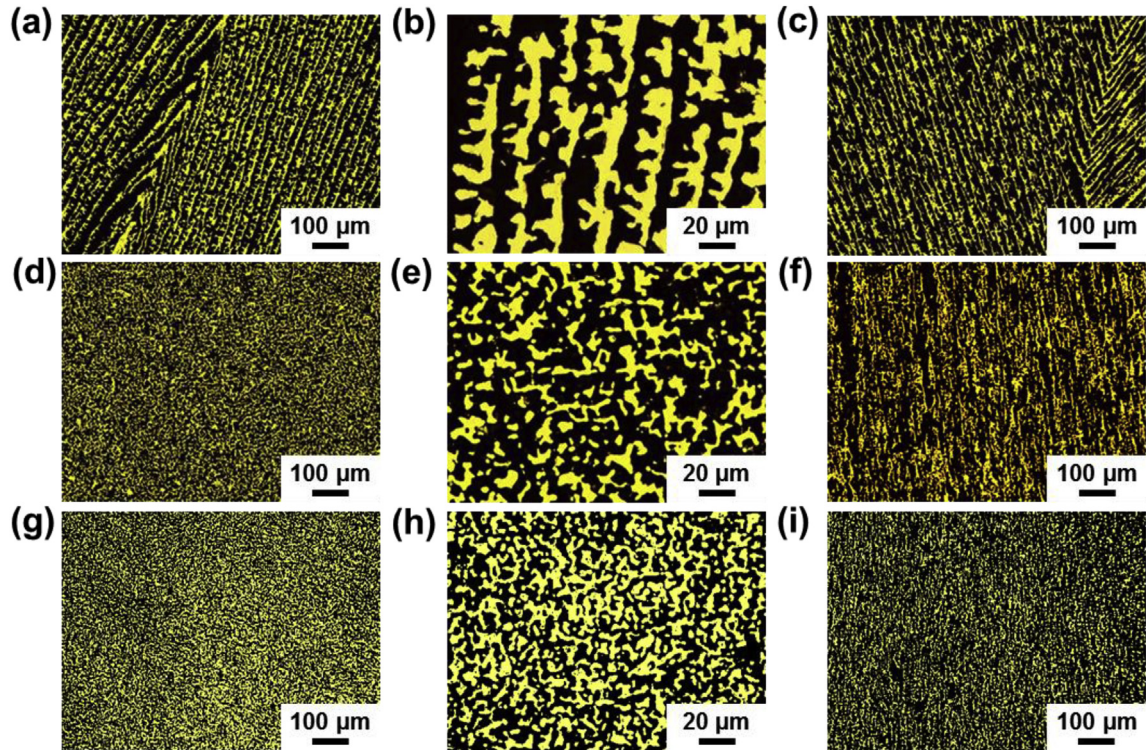
Fig. 6. Optical micrographs of radial (a, b, d, e, g, h) and longitudinal sections (c, f, i) of Co foams (Co_3O_4 powder fraction ~8 vol%; sintering time 1.5 h) with various solidification temperatures with the vertical solidification direction: (a−c) −10 °C (T10), (d−f) −30 °C (T30), and (g−i) −50 °C (T50).
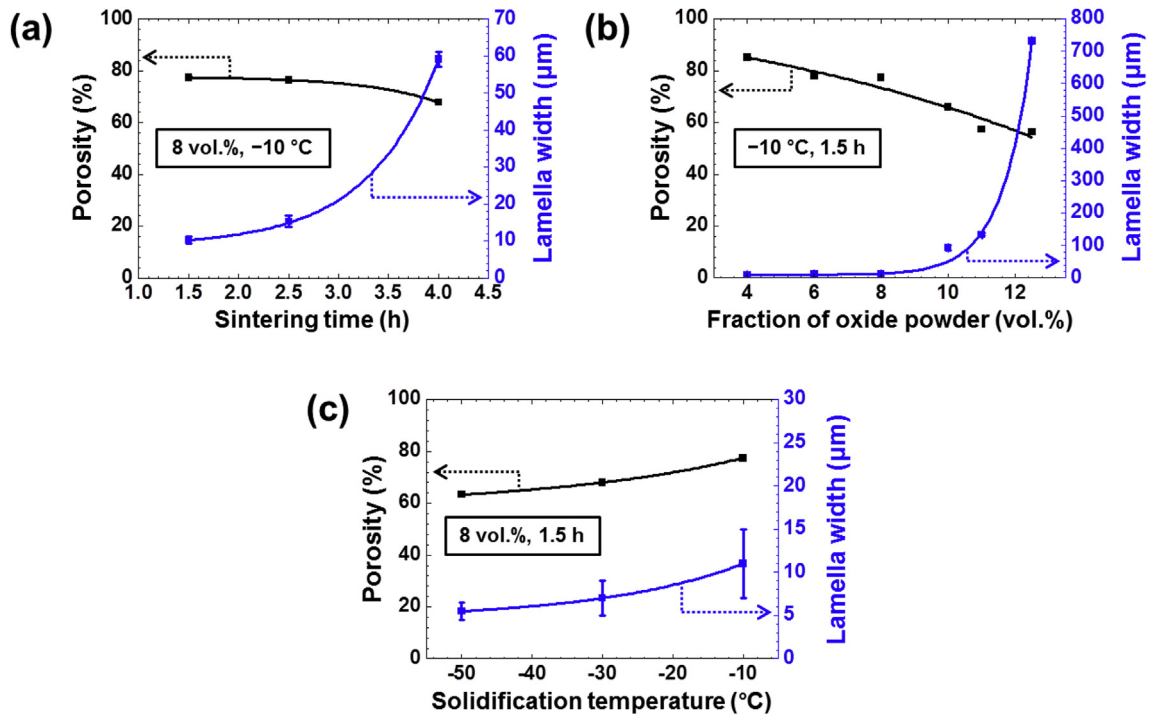
Fig. 7. Plots of Co foam porosity and lamella width against (a) sintering time (S1.5, S2.5, and S4), (b) fraction oxide powder in slurry (V4, V6, V8, V10, V11, and V12.5), and (c) solidification temperature (T10, T30, and T50).

345 MPa as the lower bound or 485 MPa as the upper bound [45]), E_{Co} is the Young's modulus of bulk Co (209 GPa [45]), ρ^* is the relative density of the Co foam, and C_1 and C_2 are constants equal to

0.3 and 1, respectively. Second, the yield strength and the Young's modulus of the C−L model are presented as described by Eqs. (3) and (4) [43].
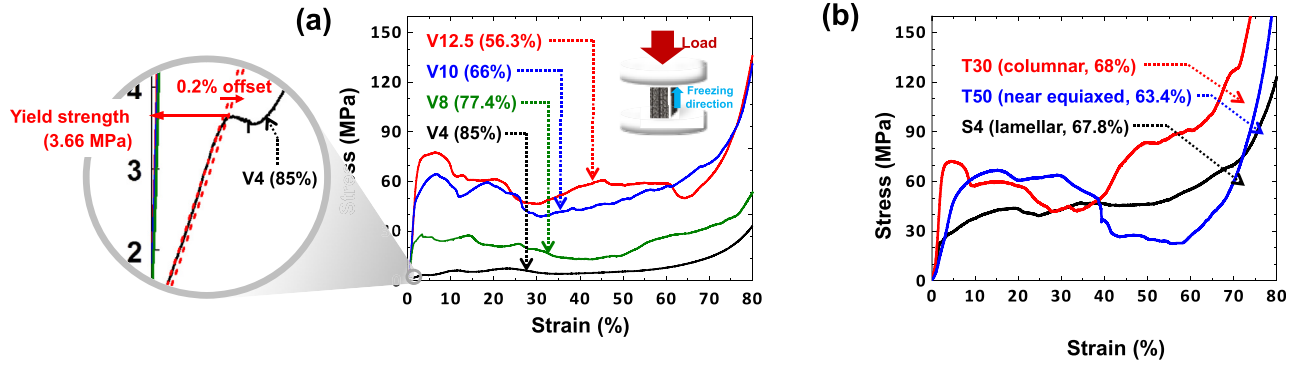
Fig. 8. Compressive stress–strain curves for Co foams with varying (a) porosities (56.3%, 66%, 77.4%, and 85%) and (b) morphologies (S4 (lamellar), T30 (columnar), and T50 (near equiaxed)) with 67.8%, 68%, and 63.4% porosity, respectively. The compressive strength was taken as the 0.2% offset yield strength.

$$\sigma^* \approx \sigma_{Co} C_3 \rho \tag{3}$$

$$E^* \approx E_{Co} C_3 \rho \tag{4}$$

where $C_3 = 0.5$ is based upon the volumetric ratio of the vertical to total struts.

In Fig. 9a, both the lower and upper bounds of yield strength prediction for bulk Co are used for comparison. Given that the ideal geometry of the G–A foam prediction model is relatively weak (strut bending), the higher experimental yield strength values in the present study appear reasonable. Indeed, experimental yield strength values being higher than the G–A prediction values has also been observed in other directionally freeze-cast metal foams (reduced from their oxides), such as Cu [16] and Fe [46]. On the other hand, the experimental yield strength values are lower than the C–L prediction values, because it is constructed based on the well-defined columnar struts with square orientation geometry and its ideal geometry is relatively strong (strut compression) [43]. However, for the present Co foams, all the experimentally measured Young's modulus values are lower than the predicted values from the G–A and C–L prediction models (Fig. 9b). This is attributed to the elastic buckling of the lamellae during the compression test, which can drastically reduce the apparent Young's modulus of macroscopic specimens. On the other hand, the yield strength can still remain high because of work hardening (for plastic buckling) or prevention of large-scale plastic buckling between neighboring lamellar colonies with different radial orientations.

3.6. Potential application of Co foam for use as an anode in LIB

Fig. 10a and b shows that a Co oxide layer with nanoscale surface roughness was successfully formed on the surface of a representative Co foam (V8: 8 vol% Co_3O_4, −10 °C) after a thermal oxidation at 600 °C, as confirmed by SEM analysis. Cross-sections of the oxidized Co foam and Co foil samples were analyzed by SEM and EDX elemental distribution profile, as displayed in Fig. 10c. The Co oxide layers were clearly observed in both the Co foam and foil samples, with the mean thickness of the oxide layer being ~500 nm. Fig. 10d shows the XRD patterns of the Co foam and foil samples with and without the thermal oxidation at 600 °C. The diffraction peaks, for both heat-treated Co foam and foil samples, verified the formation of both Co_3O_4 and CoO phases, which are known to accommodate Li ions; no diffraction peaks of any impurities were obtained.

The charge/discharge curves of the oxidized Co foam and foil samples, at a constant current of 100 mAg^{-1} with a voltage
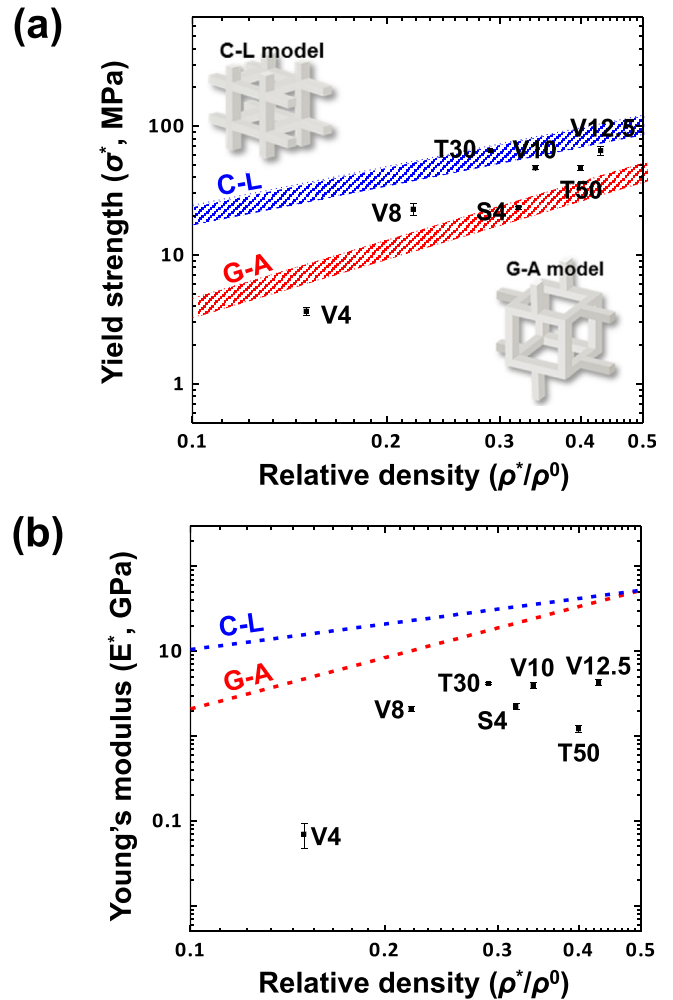
Fig. 9. Plots of (a) compressive yield strength (σ^*) versus relative density (ρ^*/ρ^0) showing measured Co foam data and the Gibson–Ashby (labeled G–A) and cellular-lattice-structure-in-square-orientation model (labeled C–L) model predictions, both for a range of Co bulk yield strength (σ_{co} = 345–485 MPa) [45]; (b) Young's modulus (E^*) versus relative density (ρ^*/ρ^0) for measured Co foam data in comparison with G–A and C–L model predictions. Error bars are based on experiments repeated in triplicate.

between 3.0 and 0.01 V, are compared between Fig. 11a and c. In the first discharge curve, a plateau of ~1 V is attributed to the reduction of Co_3O_4 and CoO to Co, as indicated in Eqs. (5) and (6). The following slope is related to the formation of a solid electrolyte
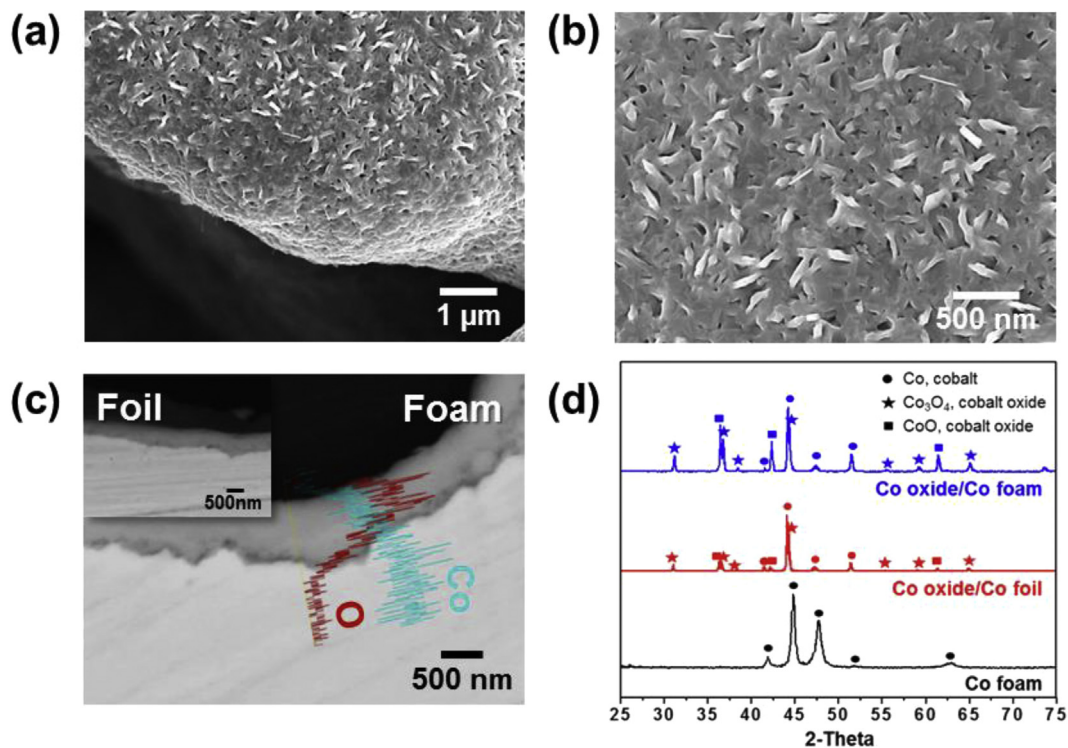
Fig. 10. SEM images of Co foam coated with active oxide (CoO/Co_3O_4) layer by thermal oxidation at 600 °C for 10 min: (a, b) surface and (c) cross-sectional morphology after mounting and polishing; additionally, the foam oxide morphology is compared with the foil oxide morphology in (c). (d) XRD patterns of Co foam before and after thermal oxidation at 600 °C for 10 min in comparison with that of Co foil with the same heat treatment.
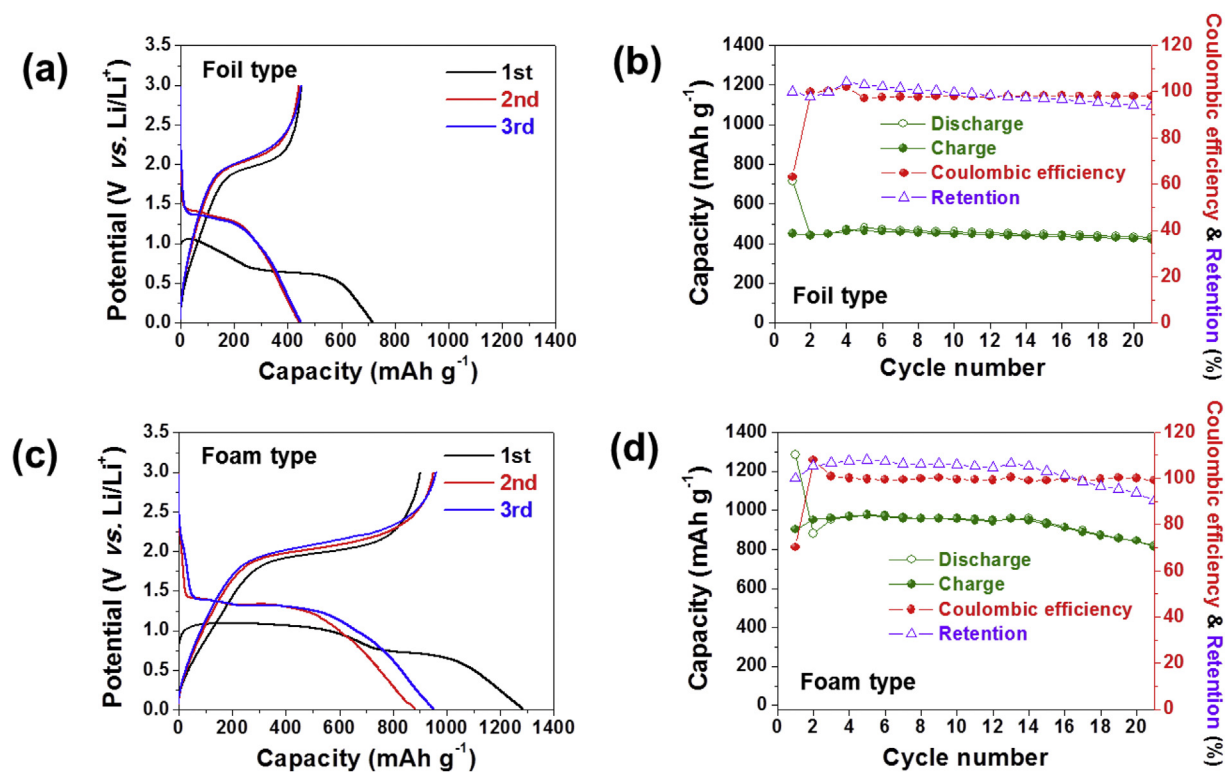
Fig. 11. Voltage profiles (a, c) and cyclic performance (b, d) of Co foil (a, b) and Co foam (c, d) with active oxide layers (CoO/Co_3O_4) grown by thermal oxidation at 600 °C for 10 min, at a constant current of 100 mAh g^{-1} in the voltage window between 3.0 and 0.01 V.

interphase (SEI) film, which can cause irreversible capacity loss [30—34].

$$Co_3O_4 + 8Li^+ + 8e^- \rightarrow 3Co + 4Li_2O \qquad (5)$$

$$CoO + 2Li^+ + 2e^- \rightarrow Co + Li_2O \qquad (6)$$
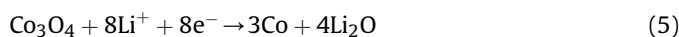
Fig. 11b and d compare the cyclic performance of the oxidized Co foam and foil samples at a constant current of 100 mAg^{-1} in the voltage between 3.0 V and 0.01 V. The initial discharge capacities (and the initial Coulombic efficiencies) were 1283 mAhg^{-1} (70.2%) and 716 mAhg^{-1} (61.6%) for the oxidized Co foam and foil samples, respectively. Remarkably, the electrochemical performance of the oxidized Co foam anode exhibited a capacity nearly twice as high as that of the oxidized foil anode, which is assigned to its larger surface area. Moreover, it showed even higher capacity than its theoretical capacity (CoO: 715 mAhg^{-1}, Co$_3$O$_4$: 890 mAhg^{-1} [30]), perhaps because it could provide more active sites, which could react with Li ions, than a typical bulk anode [31]. Additionally, a porous structure further facilitates electrolyte diffusion and accommodes volume expansion upon Li insertion/extraction [31,47—49]. In other words, the present lamellar electrode design based on oxidized Co foams with microscale aligned, lamellar pores can significantly improve the capacity and cyclic stability of the anodes of LIBs.

3.7. Effect of architecture of Co foam on the cell electrode mechanical reliability

The Co oxides − Co$_3$O$_4$ and CoO − are high-capacity anode electrode materials that can suffer from mechanical degradation caused by accumulated stresses and strains developed during (de) lithiation cycling. These accumulated stresses and strains can lead to the damage of Co-based anodes through delamination, cracking and pulverization, thus resulting in a rapid battery capacity fade [50]. Optimizing the architecture of Co foam-based anodes to improve resistance to damage is one strategy to reduce internal stresses and strains developed during (de)lithiation [35]. Here, we carry out a study of the evolution of internal stresses and strains during cyclical (dis)charging as a function of geometrical parameters by considering three cases: (i) a Co$_3$O$_4$ layer covering a smooth Co lamella, with two different thicknesses (0.5 and 0.25 μm), (ii) a Co lamella with surface roughness coated with a 0.5 μm Co$_3$O$_4$ layer, and (iii) a smooth Co lamella with internal pores coated with a 0.5 μm Co$_3$O$_4$ layer. In all cases, the solid fraction is constant, 75%, except for the case with internal pores having a solid fraction of 63%. More specifically, our previous studies [35,36] of Si- or Ni$_3$Sn$_2$-coated nickel inverse-opal anode were used as a template, as we combined a sequentially coupled diffusion and stress finite element modeling for the present case of a Co foam with a grown Co$_3$O$_4$ layer. This computational framework has been proven reliable for reproducing the internal strains observed experimentally, via x-ray diffraction, in anodes during galvanostatic cycling and (de)lithiation [35,36].

To compare the four above cases, the computed maximum von Mises stresses within the oxide layer were plotted in Fig. 12a as a function of lithiation time up to 2 h, corresponding to the full lithiation state. This maximum stress (taken as the average stress within the 10% of elements with the highest von Mises stress values in the oxide layer) is a measure of stress concentration and can be used as a criterion to determine the mechanical stability of the active layer [32—34]. Fig. 13 also shows, for the four cases, the computed von Mises stress distributions of the oxide layers after the full lithiation state (2 h).

Stress accumulation in the thick oxide layer occurs faster than in thin oxide layer, indicating that more oxidized Co foams, where the
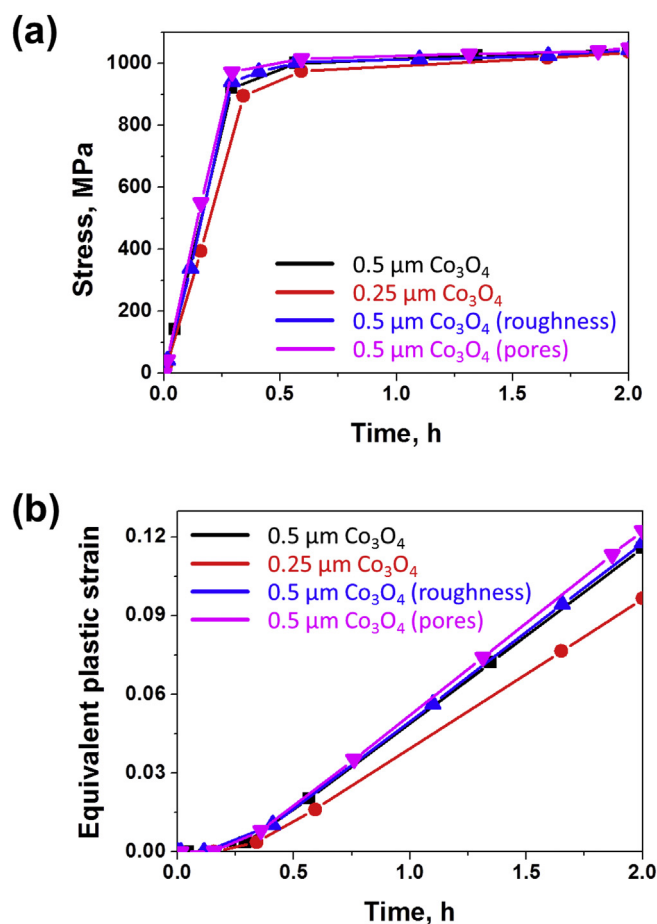
Fig. 12. Comparison of evolution during the lithiation process, for the four cases shown in Fig. 2, of (a) the computed maximum von Mises stress (averaged over the 10% of elements with the highest von Mises values in the oxide layer) and (b) the computed equivalent plastic strain evolutions in the oxide layers.

oxide layer is thicker and the Co scaffold thinner, are more prone to damage, due to higher lithiation-induced internal stresses in the oxide layer which make it less mechanically stable. As seen in Fig. 13, each of the four cases shows a similar von Mises stress distribution, with stress concentrated at the connecting regions between lamella and bridge where mechanical damage and cracking are thus more likely to occur. As seen in Fig. 12a, roughness in the Co foam slightly increased the maximum von Mises values of the oxide layer, because the surface roughness likely provided sources of stress accumulation as illustrated in Fig. 13. Additionally, the stress accumulation of the Co foam with pores in the lamella and a thicker oxide layer was slightly steeper than that of the Co foam with a pore-free lamella (and the same thicker oxide layer); this may be explained by the lower Co fraction due to the presence of pores within the lamella, resulting in a scaffold more prone to elastic deformation and thus higher stress accumulation in the oxide layer [44].

The volume-averaged von Mises (equivalent) plastic strain from each element in the oxide layer was plotted as a function of lithiation time, as shown in Fig. 12b. The four cases showed similar onsets of plasticity, indicating that yielding in the oxide layer started at about 0.3 h in all four cases. The plastic strain accumulation was essentially the same in the three thicker oxide layers, but somewhat lower (by ~25%) in the thinner oxide layer. The plastic strain accumulation of the Co foam with a thicker oxide layer and the presence of pores was slightly steeper. Thus, this analysis indicates that plastic strain accumulation in the Co oxide layer during
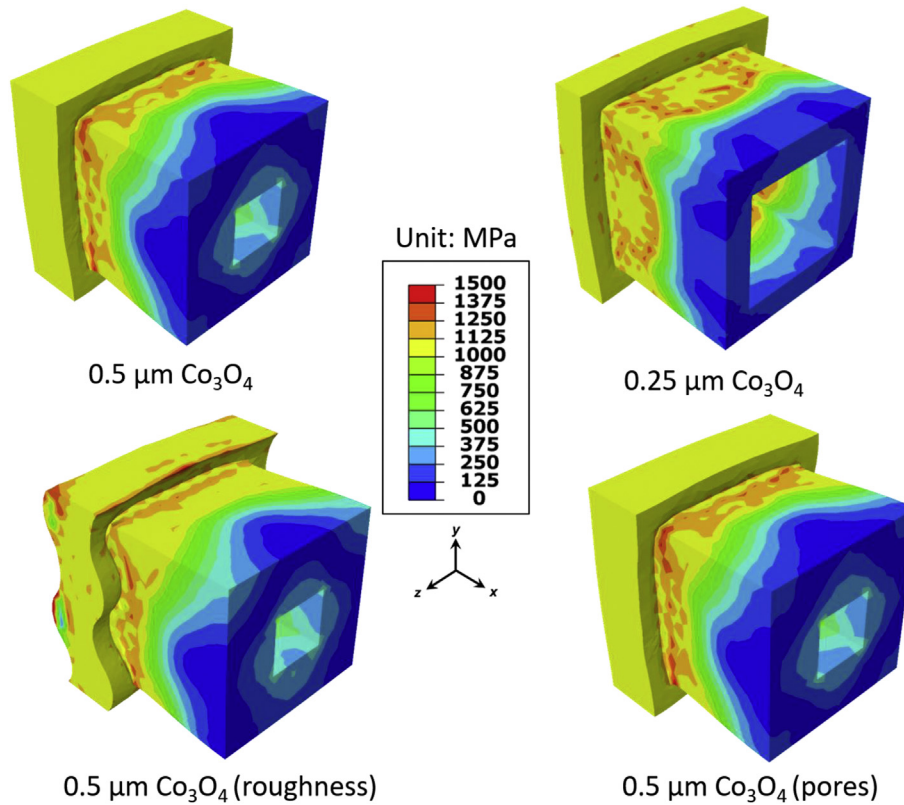
Fig. 13. Computed von Mises stress distributions of the oxide layers, for the four cases shown in Fig. 2, at the full lithiation state.

lithiation is sensitive to the thickness of the active oxide layer, but barely so to the metal/oxide interface roughness and the presence of pores in the metallic lamellae.

4. Conclusions

Cobalt foams, with porosities between 56 and 85% and aligned lamellar pores of a few tens of microns (10−50 μm) in width and ~8 mm in height, were created via an ice-templating method: Co_3O_4 nanoparticles aqueous slurries were directionally solidified to create aligned ice dendrites surrounded by lamellae enriched in Co_3O_4, the ice was removed by sublimation, and the templated Co_3O_4 structure was reduced to Co and sintered. The following conclusions were drawn:

1. Microstructural changes were achieved by controlling the three main processing parameters: slurry solidification temperature (and thus solidification velocity), powder fraction in the slurry and sintering time.
   (i) During the initial stage of sintering, the internal pores within the lamellae were eliminated, prior to the thickening of the lamellae. The Co lamella surfaces are smooth on one side and corrugated on the other, creating secondary surface pores, as a result of short secondary dendrite arms.
   (ii) Increasing the sintering time from 1.5 to 2.5 h increases the Co lamella thickness from 10.3 ± 0.9 to 15.3 ± 1.5 μm. As sintering time was increased from 2.5 to 4 h a near quadrupling of lamella thickness (from 15.3 ± 1.5 to 59.1 ± 2 μm) occurs, suggesting that neighboring lamellae coalesced and sintered together.
   (iii) The porosity of the Co foams decreased from 85.1 to 56.3% for Co_3O_4 powder slurry concentrations increasing from 4

   to 12.5 vol%. The foams solidified from slurries with higher volume fractions of Co_3O_4 nanoparticles (10, 11, and 12.5 vol%) showed much thicker Co lamellae with smaller irregularly distributed pores in thick struts. Lamella coalescence appeared to be responsible for the drastic increase in lamella thickness (from 11 to 93 μm) as slurry Co_3O_4 fraction increased modestly from 8 to 10 vol%.
   (iv) Solidification temperature was varied from −10 to −50 °C, which resulted in differences in morphology in both the radial and longitudinal directions. A finer microstructure (smaller pores and thinner lamella struts) was achieved with a lower solidification temperature and faster freezing rate.
2. The Co foams exhibited compressive deformation behavior typical of ductile porous metals. With porosity decreasing from 85 to 56.3%, the compressive yield strength of the Co foam increased from 4 to 64 MPa. The experimental values of yield strength and Young's modulus were compared with the Gibson−Ashby and cellular−lattice−structure−in−square−orientation models, which do not take into account the complex microstructure observed here (porous lamellae which are misoriented with respect to load and may show plastic buckling).
3. Thermal oxidation of the Co foam created an integrated Co_3O_4/CoO/Co foam anode for lithium ion batteries (LIB). A cyclic lithium charge/discharge test of this integrated foam anode showed that the initial discharge capacity and Coulombic efficiency were 1283 mAhg^{-1} (twice as high as that of a control Co_3O_4/CoO/Co foil anode) and 70.2%, respectively. Owing to its large surface area and expected low processing cost, such Co_3O_4/CoO/Co foams are promising candidates for self-supporting integrated anodes for high capacity LIBs.
4. Finite element modeling was used to compute von Mises stress and equivalent plastic strain evolutions in the oxide layers of Co

foams during lithiation; four different geometries (two oxide layer thickness and the presence of pores or surface roughness in the Co lamellae) were considered, and only the difference in oxide thickness created a sizeable difference in the mechanical response of the oxide layer during the lithiation process.

Acknowledgments

Appendix A. Supplementary data

Supplementary data related to this article can be found at https://doi.org/10.1016/j.actamat.2017.09.066.

References

[1] Q. Liu, J. Coakeley, D.N. Seidman, D.C. Dunand, Precipitate evolution and creep behavior of a W-Free Co-based superalloy, Metall. Mater. Trans. A 47 (2016) 6090–6096.

[2] K.M. Mantrala, M. Das, V.K. Balla, C.S. Rao, V.V.S. Kesava Rao, Additive manufacturing of Co-Cr-Mo alloy: influence of heat treatment on microstructure, tribological, and electrochemical properties, Front. Mech. Eng. 1 (2015) 1–7.

[3] Akane Suzuki Haruyuki Inui, Tresa M. Pollock, L12-strengthened cobalt-base superalloys, Annu. Rev. Mater. Res. 45 (2015) 345–368.

[4] J. He, J.M. Schoenung, A review on nanostructured WC-Co coatings, Surf. Coat. Technol. 157 (2002) 72–79.

[5] Y. Surendranath, M. Dincă, D.G. Nocera, Electrolyte-dependent electrosynthesis and activity of cobalt-based water oxidation catalysts, J. Am. Chem. Soc. 131 (2009) 2615–2620.

[6] J.D. Blakemore, N.D. Schley, D. Balcells, J.F. Hull, G.W. Olack, C.D. Incarvito, O. Eisenstein, G.W. Brudvig, R.H. Crabtree, Half-sandwich iridium complexes for homogeneous water-oxidation catalysis, J. Am. Chem. Soc. 132 (2010) 16017–16029.

[7] Y. Noh, K. Yoo, J.Y. Kim, O. Song, M.J. Ko, Iridium catalyst based counter electrodes for dye-sensitized solar cells, Curr. Appl. Phys. 13 (2013) 1620–1624.

[8] H. Su, H. Chen, F. Fang, C. Liu, C. Wu, K. Wong, Y. Liu, S. Peng, Solid-state white light-emitting electrochemical cells using iridium-based cationic transition metal complexes, J. Am. Chem. Soc. 130 (2008) 3413–3419.

[9] M.F. Ashby, A.G. Evans, N.A. Fleck, L.J. Gibson, J.W. Hutchinson, H.N.G. Wadley, Metal Foams: a Design Guide, Butterworth-Heinemann, Boston, MA, 2000.

[10] J. Banhart, Manufacture, characterization and application of cellular metals and metal foams, Prog. Mater. Sci. 46 (2001) 559–632.

[11] L.-P. Lefebvre, J. Banhart, D.C. Dunand, Porous metals and metallic foams: current status and recent developments, Adv. Eng. Mater 10 (2008) 775–787.

[12] G.J. Davies, S. Zhen, Metallic foams: their production, properties and applications, J. Mater. Sci. 18 (1983) 1899–1911.

[13] S. Deville, C. Viazzi, J. Leloup, A. Lasalle, C. Guizard, E. Maire, J. Adrien, L. Gremillard, Ice shaping properties, similar to that of antifreeze proteins, of a zirconium acetate complex, PLoS One 6 (10) (2011) 1–6 e26474.

[14] S. Deville, Freeze-casting of porous ceramics: a review of current achievements, Adv. Eng. Mater 10 (2008) 155–169.

[15] K.L. Scotti, E.E. Northard, A. Plunk, B.C. Tappan, D.C. Dunand, Directional solidification of aqueous TiO2 suspensions under reduced gravity, Acta Mater 124 (2017) 608–619.

[16] H. Park, M. Choi, H. Choe, D.C. Dunand, Microstructure and compressive behavior of ice-templated copper foams with directional, lamellar pores, 679 Mater. Sci. Eng. A (2017) 435–445.

[17] S.M. Miller, X. Xiao, K.T. Faber, Freeze-cast alumina pore networks: effects of freezing conditions and dispersion medium, J. Eur. Ceram. Soc. 35 (2015) 3595–3605.

[18] Y. Chino, D.C. Dunand, Directionally freeze-cast titanium foam with aligned, elongated pores, Acta Mater 56 (2008) 105–113.

[19] S. Deville, E. Saiz, A.P. Tomsia, Freeze casting of hydroxyapatite scaffolds for bone tissue engineering, Biomaterials 27 (2006) 5480–5489.

[20] M.E. Launey, E. Munch, D.H. Alsem, H.B. Barth, E. Saiz, A.P. Tomsia, R.O. Richie, Designing highly toughened hybrid composites through nature-inspired hierarchical complexity, Acta Mater 57 (2009) 2919–2932.

[21] S. Deville, E. Saiz, R.K. Nalla, A.P. Tomsia, Freezing as a path to build complex composites, Science 311 (2006) 515–518.

[22] N.O. Shanti, K. Araki, J.W. Halloran, Particle redistribution during dendritic solidification of particle suspensions, J. Am. Ceram. Soc. 89 (2006) 2444–2447.

[23] J.C. Li, D.C. Dunand, Mechanical properties of directionally freeze-cast titanium foams, Acta Mater 59 (2011) 146–158.

[24] H. Jo, M. Kim, H. Choi, Y.-E. Sung, H. Choe, D.C. Dunand, Morphological study of directionally freeze-cast nickel foams, Metall. Mater. Trans. E 3 (2016) 46–54.

[25] S. Deville, S. Meille, J. Seuba, A meta-analysis of the mechanical properties of ice-templated ceramics and metals, Sci. Technol. Adv. Mater 16 (2015) 043501.

[26] R. Sepulveda, A.A. Plunk, D.C. Dunand, Microstructure of Fe2O3 scaffolds created by freeze-casting and sintering, Mater. Lett. 142 (2015) 56–59.

[27] A. Röthlisberger, S. Häberli, R. Spolenak, D.C. Dunand, Synthesis, structure and mechanical properties of directionally freeze-cast tungsten foams, J. Mater. Res. 31 (2016) 753–764.

[28] A.E. Jakus, S.L. Taylor, N.R. Geisendorfer, D.C. Dunand, R.N. Shah, Metallic architectures from 3D-printed powder-based liquid inks, Adv. Funct. Mater 25 (2015) 6985–6995.

[29] Y.S. Kim, S.I. Cha, S.H. Hong, Nanoporous cobalt foam and a Co/Co(OH)2 core-shell structure for electrochemical applications, J. Mater. Chem. A 1 (2013) 9802–9808.

[30] L. Zhang, P. Hu, X. Zhao, R. Tian, R. Zou, D. Xia, Controllable synthesis of core–shell Co@CoO nanocomposites with a superior performance as an anode material for lithium-ion batteries, J. Mater. Chem. 21 (2011) 18279–18283.

[31] N. Yan, L. Hu, Y. Li, H. Zhong, X. Hu, X. Kong, Q. Chen, Co3O4 nanocages for high-performance anode material in lithium-ion batteries, J. Phys. Chem. C 116 (2012) 7227–7235.

[32] Y. Fu, X. Li, X. Sun, X. Wang, D. Liu, D. He, Self-supporting Co3O4 with lemongrass-like morphology as a high-performance anode material for lithium ion batteries, J. Mater. Chem. 22 (2012) 17429–17431.

[33] G. Huang, S. Xu, S. Lu, L. Li, H. Sun, Micro-Nanostructured Co3O4 anode with enhanced rate capability for lithium-ion batteries, ACS Appl. Mater. Interfaces 6 (2014) 7236–7243.

[34] J.S. Do, C.H. Weng, Preparation and characterization of CoO used as anodic material of lithium battery, J. Power Sources 146 (2005) 482–486.

[35] H.H. Cho, M.P.B. Glazer, D.C. Dunand, Modeling of stresses and strains during (de)lithiation of Ni3Sn2-coated nickel inverse-opal anodes, ACS Appl. Mater. Interfaces 9 (18) (2017) 15433–15438.

[36] H.H. Cho, M.P.B. Glazer, Q. Xu, H.N. Han, D.C. Dunand, Numerical and experimental investigation of (de)lithiation-induced strains of bicontinuous silicon-coated nickel inverse opal anodes, Acta Mater 107 (2016) 289–297.

[37] E. Munch, E. Saiz, A.P. Tomsia, S. Deville, Architectural control of freeze-cast ceramics through additives and templating, J. Am. Ceram. Soc. 92 (2009) 1534–1539.

[38] S. Deville, E. Saiz, A.P. Tomsia, Ice-templated porous alumina structures, Acta Mater 55 (2007) 1965–1974.

[39] A.M. Anderson, M.G. Worster, Periodic ice banding in freezing colloidal dispersions, Langmuir 28 (2012) 16512–16523.

[40] A. Lasalle, C. Guizard, E. Maire, J. Adrien, S. Deville, Particle redistribution and structural defect development during ice templating, Acta Mater 60 (2012) 4594–4603.

[41] W.L. Li, K. Lu, J.Y. Walz, Freeze casting of porous materials: review of critical factors in microstructure evolution, Int. Mater. Rev. 57 (2012) 37–60.

[42] H. Park, Y. Noh, H. Choi, K. Hong, K. Kwon, H. Choe, Processing, microstructure, and oxidation behavior of iron foams, Metall. Mater. Trans. A 47 (2016) 4760–4766.

[43] E. Hong, B.Y. Ahn, D. Shoji, J.A. Lewis, D.C. Dunand, Microstructure and mechanical properties of reticulated titanium scrolls, Adv. Eng. Mater 13 (2011) 1122–1127.

[44] L.J. Gibson, M.F. Ashby, Cellular Solids: Structures and Properties, Cambridge University Press, NY, 1997.

[45] E.A. Brandes, G.B. Brook, Smithells Metals Reference Book, seventh ed., Butterworth-Heinemann, Oxford, UK, 1992.

[46] A.A. Plunk, D.C. Dunand, Iron foams created by directional freeze casting of iron oxide, reduction and sintering, Mater. Lett. 191 (2017) 112–115.

[47] H. Park, J.-H. Um, M. Choi, Y.-E. Sung, H. Choe, Hierarchical micro-lamella-structured 3D porous copper current collector coated with tin for advanced lithium-ion batteries, Appl. Surf. Sci. 399 (2017) 132–138.

[48] J.H. Um, M. Choi, H. Park, Y.-H. Cho, D.C. Dunand, H. Choe, Y.-E. Sung, 3D macroporous electrode and high-performance in lithium-ion batteries using SnO2 coated on Cu foam, Sci. Rep. 6 (2016) 18626.

[49] H. Park, H. Choi, K. Nam, S. Lee, J. Um, K. Kim, J.H. Kim, W.S. Yoon, H. Choe, Anode design based on microscale porous scaffolds for advanced lithium ion batteries, J. Electron. Mater 46 (2017) 3789–3795.

[50] P. Arora, R.E. White, M. Doyle, Capacity fade mechanisms and side reactions in lithium-ion batteries, J. Electrochem. Soc. 145 (1998) 3647–3667.